Journal of Solid State Chemistry 183 (2010) 649–657

Contents lists available at ScienceDirect

Journal of Solid State Chemistry

journal homepage: www.elsevier.com/locate/jssc

Interactions of $Ba_2YCu_3O_{6+y}$ with the Gd_3NbO_7 buffer layer in coated conductors

W. Wong-Ng [a,*], Z. Yang [a,1], J.A. Kaduk [b], L.P. Cook [a], M. Paranthaman [c]

[a] Ceramics Division, National Institute of Standards and Technology, Gaithersburg, MD 20899
[b] INEOS Technology, Naperville, IL 60566-7011
[c] Oak Ridge National Laboratory, Oak Ridge, TN 37831

ARTICLE INFO

Article history:
Received 5 November 2008
Received in revised form
25 December 2009
Accepted 10 January 2010
Available online 18 January 2010

Keywords:
Superconductors
$Ba_2YCu_3O_{6z}$ and Gd_3NbO_7 interactions
Structure of $Ba2(G_{dx}Y_{1-x})NbO_6$ and $(Gd_xY_{3-x})NbO_7$
Reference X-ray powder patterns

ABSTRACT

A systematic study of the chemical interaction of $Ba_2YCu_3O_{6+y}$ and Gd_3NbO_7 was conducted under two processing conditions: purified air (21% p_{o_2}), and 100 Pa p_{o_2} (0.1% p_{o_2}). Phases present along the pseudo-binary join $Ba_2YCu_3O_{6z}$ and Gd_3NbO_7 were found to be in two five-phase volumes within the $BaO-\frac{1}{2}Y_2O_3-\frac{1}{2}Gd_2O_3-Nb_2O_5-CuO_y$ system. Three common phases that are present in all samples are $(Y,Gd)_2Cu_2O_5$, $Ba(Y,Gd)_2CuO_5$ and Cu_2O or CuO (depending on the processing conditions). The assemblies of phases can be categorized in three regions, with $Ba_2YCu_3O_{6+y}$: Gd_3NbO_7 ratios of (I) < 5.5:4.5; (II)=5.5:4.5; and (III) > 5.5:4.5. The lowest melting temperature of the system was determined to be ≈938 °C in air, and 850 °C at 100 Pa p_{o_2}. Structure determinations of two selected phases, $Ba_2(Gd_xY_{1-x})NbO_6$ ($Fm\bar{3}m$, No. 225), and $(Gd_xY_{3-x})NbO_7$ ($C222_1$, No. 20 and *Ccmm*, No. 63), were completed using the X-ray Rietveld refinement technique. Reference X-ray powder diffraction patterns for selected phases of $Ba_2(Gd_xY_{1-x})NbO_6$ (x=0.2, 0.4, 0.6, and 0.8) and $(Gd_xY_{3-x})NbO_7$ (x=0.6, 1.2, 1.8, 2.4 and 3) have been prepared for inclusion in the Powder Diffraction File (PDF).

1. Introduction

In the last few years, a large part of high-temperature superconductor research has focused on coated conductor technology [1–4], a technology which has considerable promise for commercialization. Global efforts in research and development on every aspect of the technology, including phase formation mechanisms, flux pinning/J_c (critical current density) relationships, and buffer layer architecture, are underway.

Coated conductors consist of superconductor-coated metallic substrates with multilayered buffers in between the substrate and the superconductor film. At the present time, coated conductors are based primarily on $Ba_2YCu_3O_{6+y}$ (Y-213) and $Ba_2RCu_3O_{6+y}$ (R=lanthanides) as the superconducting materials. The general functions of the buffer layers are to provide protection and physical/chemical barriers for the superconductor layers, and above all, to provide texture for crystallographic alignment. The phases $SrTiO_3$ and CeO_2 are extensively used as buffer layers immediately below the superconductor layer [5,6]. Additionally, Gd_3NbO_7 is a possible choice for a single-layer buffer in coated conductors produced with RABiTS technology [3,4] using pulsed laser deposition (PLD). The use of Gd_3NbO_7 considerably simplifies the buffer architecture.

The incorporation of buffer layers into coated conductor technology provides many benefits, including the promotion of epitaxial growth of $Ba_2YCu_3O_{6+y}$. However, there may be unavoidable reactions at the interface between layers. Understanding interfacial reactions of the *Y*-213 phase with buffer layers is essential to avoid and/or control the formation of undesirable phases. This understanding is best achieved by reference to the appropriate phase diagrams, which have direct application to the interpretation of results of transmission electron microscopy (TEM) and scanning electron microscopy (SEM) of coated conductor interfaces. The main goal of this paper is to summarize our recent experimental studies of the multi-component phase equilibria relevant to the interactions between $Ba_2YCu_3O_{6+y}$ and Gd_3NbO_7. For these studies, we have relied extensively on X-ray diffraction and differential thermal analysis/thermal gravimetric analysis (DTA/TGA).

Another goal of this paper is to determine the crystal chemistry and crystallography of selected reaction product phases, $Ba_2(Gd_xY_{1-x})NbO_6$ and $(Gd_xY_{3-x})NbO_7$, including the preparation of the standard reference X-ray patterns of selected $Ba_2(Gd_xY_{1-x})NbO_6$ (x=0.2, 0.4, 0.6, and 0.8) and $(Gd_xY_{3-x})NbO_7$ (x=0.6, 1.2, 1.8, 2.4, and 3) solid solution members. Two structure types for Ba_2RNbO_6 have been reported in literature, corresponding to the cubic and tetragonal Ba_2EuNbO_6 structure [7,8].

* Corresponding author.
E-mail address: Winnie.wong-ng@nist.gov (W. Wong-Ng).
[1] Present address: Chemistry Department, Yunnan Normal University, Kunming 650092, PR China.

0022-4596/$ - see front matter © 2010 Published by Elsevier Inc.
doi:10.1016/j.jssc.2010.01.006

R_3NbO_7 was reported to crystallize in a number of different space groups. For example, Allpress and Rossell [9] reported the R=La analog crystallizes in the fluorite-related *Cmcm* structure, and those with smaller size R^{3+} (R=Nd, Gd, Ho and Y) adopt the superstructure space group of $C222_1$. Garton gave a hexagonal structure (a=6.51 Å and c=18.81 Å) for Gd_3NbO_7 [10]. Sirotinkin and Wanklyn [11], on the other hand, found the analogs with R=Dy, Ho, Y, Er, Tm and Yb to be cubic while the R_3NbO_7 compounds with larger size of R^{3+} (La, Pr, Nd, Sm, Gd, Tb) crystallize in the orthorhombic fluorite-type structure. The $Fm\bar{3}m$ space group has also been reported by Rooksby and White for both Y_3NbO_7 and Gd_3NbO_7 [12]. Other structures reported for Gd_3NbO_7 included the high temperature *Cmcm* [13] and the orthorhombic *Pnma* [14] structures.

2. Experimental[2]

2.1. Preparation of samples in the $Ba_2YCu_3O_{6+y}$–Gd_3NbO_7 system

Two master batches of $Ba_2YCu_3O_{6+y}$ and Gd_3NbO_7 were first processed, then individual compositions with different ratios of $Ba_2YCu_3O_{6+y}$ and Gd_3NbO_7 were prepared from these master batches. To prepare $Ba_2YCu_3O_{6+y}$, stoichiometric amounts of BaO, Y_2O_3 and CuO were weighed out, well-mixed and calcined in an atmospherically controlled high temperature furnace, repeatedly, first at 850 °C, then at 930 °C, with intermediate grindings, for about 2 weeks. To prepare Gd_3NbO_7, a stoichiometric amount of Gd_2O_3 and Nb_2O_5 was mixed, pressed into pellets, and then heat-treated from 850 °C to the highest of 1470 °C for a total of one week with intermediate grindings. The operations of sample weighing, sample homogenization and pellet-pressing were performed inside a glove-box. Pelletized samples were placed inside individual MgO crucibles for annealing in a horizontal box-type controlled-atmosphere furnace. Transfer from the glove-box to the box furnace and *vice-versa* was achieved via a second transfer vessel and an interlock system attached to the furnace.

Nine samples with $Ba_2YCu_3O_{6+y}$/Gd_3NbO_7 ratio of 1:9, 2:8, 3:7, 4:6, 5:5, 6:4, 7:3, 8:2, 9:1 were prepared under atmospherically controlled conditions in both purified air (0.21 MPa p_{O_2} (21% O_2), 930 °C), and 100 Pa p_{O_2} (0.1% O_2 (balance argon), 810 °C). The air was purified by using in-line CO_2 and H_2O scrubbers. During the heat-treatment process, the oxygen partial pressure of the Ar/O_2 mixture was controlled to the specified value using a mass flow meter, and monitored at both the inlet and outlet of the furnace using a zirconia oxygen sensor. Intermediate grindings and pelletizations took place until no further changes were detected in the powder X-ray diffraction patterns.

To perform structural characterization of reaction products, we have also prepared two solid solution series, $Ba_2(Gd_xY_{1-x})NbO_6$ (x=0.2, 0.4, 0.6, and 0.8) and $(Gd_xY_{3-x})NbO_7$ (x=0.6, 1.2, 1.8, 2.4, and 3.0). Samples were prepared in air using stoichiometric amounts of Gd_2O_3, Y_2O_3, and Nb_2O_5 as the starting reagents. The heat treatment process was initiated at 850 °C, with increments to 1470 °C, with intermediate grindings, for a total of one week.

2.2. Phase analysis

X-ray powder diffraction was used to identify the phases synthesized, to confirm phase purity, and to determine phase relationships. A computer-controlled automated Philips diffractometer equipped with a θ-compensation slit and Cu$K\alpha$ radiation was operated at 45 kV and 40 mA. The radiation was detected by a scintillation counter and a solid-state amplifier. All X-ray patterns were measured using a hermetic cell designed for air-sensitive materials [15]. The Siemens software package and the reference X-ray diffraction patterns of the Powder Diffraction File (PDF) [16] were used for performing phase identification.

2.3. Structure studies using diffraction techniques

To study the structure and prepare reference X-ray powder diffraction patterns for the $Ba_2YCu_3O_{6+y}$/Gd_3NbO_7 reaction products, the X-ray Rietveld refinement technique (GSAS Suite) [17–19] was applied. The specimens were mounted as acetone slurries on zero-background cells, and were rotated rapidly during data collections. All data processing and Rietveld structural refinements were carried out using the GSAS Suite [17–19]. The structure of $Ba_2(Gd_xY_{1-x})NbO_6$ and $Gd_{3-x}Y_xNbO_7$ was determined using a Bruker XRD D8 Advance Diffractometer equipped with a VANTEC-1 position-sensitive detector. Diffraction patterns were collected from 5–150° 2θ using Ni-filtered Cu$K\alpha$ radiation, 0.00729689°/step and 1 s/step. For the study of the structure of $(Gd_xY_{3-x})NbO_7$, additional high resolution powder patterns (higher signal/noise and lower background) were collected at ambient conditions (5–140°, 0.01313° steps, 6 sec/step) on a PANalytical X'Pert Pro MPD diffractometer equipped with a PIXcel position-sensitive detector, a diffracted beam monochromator, and an Anton Paar HTK1200N furnace.

2.3.1. $Ba_2(Gd_xY_{1-x})NbO_6$

To determine the crystal system and space group for the $Ba_2(Gd_xY_{1-x})NbO_6$ perovskites, five possible space groups in the PDF [16] that have been reported for their related phases, namely, $Fm\bar{3}m$ (No. 225), $I4/m$ (No. 87), $Pm\bar{3}m$ (No. 221), $I4/mcm$ (No. 140) and $P2_1/n$ (No. 14) have been used to first refine the solid solution member $Ba_2Gd_{0.4}Y_{0.6}NbO_6$ (Table 1). In the $Pm3m$ and $I4/mcm$ models, the Gd, Y, and Nb occupy the same site, resulting in unreasonable bond valence sums value, V_b (calculated using the Brown-Altermatt empirical expression (Table 1) [20,21]. V_b of an atom i is defined as the sum of the bond valences v_{ij} of all the bonds from atoms i to atoms j. The most commonly adopted empirical expression for the bond valence v_{ij} as a function of the interatomic distance d_{ij} is $v_{ij}=\exp[(R_0-d_{ij})/B]$. The parameter, B, is commonly taken to be a "universal" constant equal to 0.37 Å. The values of the reference distance R_0 for Ba–O, Nb–O, Gd–O and Y–O

Table 1
Refinement residuals for $Ba_2Gd_{0.4}Y_{0.6}NbO_6$.

Space Group, SG	$Fm\bar{3}m$	$Pm3m$	$I4/mcm$	$I4/m$	$P2_1/n$
SG #	225	221	140	87	14
RW_p	0.0550	0.0552	0.0545	0.0544	~0.0545
R_p	0.0428	0.0430	0.0428	0.0425	~0.0428
χ^2	2.410	2.420	2.365	2.365	~2.365
% χ^2 from restraints	0.08	0	0	0.51	~0.04
# Variables	19	17	19	21	33
# Observ.	18504	18498	18498	18504	18504
$R(F)$	0.0954	0.0646	0.0781	0.0926	~0.1477
$R(F^2)$	0.0919	0.3084	0.0843	0.0746	~0.0732
ΔF, +	3.7	2.5	2.8	3.1	4.2
ΔF, −	−2.2	−2.4	−2.3	−2.5	−4.9
V_b					
Gd	3.82	5.27	5.21	3.98	
Y	3.33	4.59	4.54	3.47	
Nb	4.78	3.47	3.44	4.60	

[2] Certain trade names and company products are mentioned in the text or identified in illustrations in order to adequately specify the experimental procedures and equipment used. In no case does such identification imply recommendation or endorsement by the National Institute of Standards and Technology.

are 2.285, 1.911, 2.065 and 2.014 Å, respectively. Therefore the *Pm*3*m* and *I*4/*mcm* models can be discarded as chemically-unreasonable. The $P2_1/n$ model did not converge, indicating that this symmetry is not supported by the data. The *I*4/*m* model converged slowly with a high damping factor of 8 for the structural parameters. The *I*4/*m* model and the $Fm\bar{3}m$ models were then used for the refinements and comparison of all four $Ba_2(Gd_xY_{1-x})NbO_6$ compounds.

2.3.2. $Gd_{3-x}Y_xNbO_7$

The study of the structure of $Gd_{3-x}Y_xNbO_7$ was more challenging. The powder patterns of the $Gd_{3-x}Y_xNbO_7$ series collected using the Bruker diffractometer fall into two classes. The best match to the patterns of the three Gd-rich samples ($Gd_{1.8}Y_{1.2}NbO_7$, $Gd_{2.4}Y_{0.6}NbO_7$, and Gd_3NbO_7) that have obvious superlattice peaks is PDF 04-010-0648, from the $C222_1$ structure [16]. The patterns of the two Y-rich samples ($Gd_{1.2}Y_{1.8}NbO_7$ and $Gd_{0.6}Y_{2.4}NbO_7$), which do not exhibit the obvious weak orthorhombic superstructure peaks are matched best by patterns of *fcc* phases (a=5.25 Å, $Fm\bar{3}m$; PDF 01-074-6421 [16]). However, the $Fm\bar{3}m$ Y_3NbO_7 structure has 8 M–O bonds at 2.271 Å. This environment yields an unreasonable V_b value of 3.99, 4.58, and 3.02 for Y, Gd, and Nb, respectively. The structure thus does not seem to be chemically plausible. Furthermore, refinement of the $Gd_{0.6}Y_{2.4}NbO_7$ structure in the $Fm\bar{3}m$ space group, although yielding a statistically-better refinement than in $C222_1$ (χ^2=2.137 and 3.249 for $Fm\bar{3}m$ and $C222_1$, respectively), it comes at the cost of unreasonable displacement coefficients, U_{iso} ($Fm\bar{3}m$: U_{iso} (Gd,Y)=0.0303(1) Å^2, U_{iso} (O)=0.0804(9) Å^2; $C222_1$: U_{iso} (Nb)=0.0176(10), and U_{iso} (O)=0.0327(17) Å^2). It is understandable that at high *Y* concentrations, the electron populations at the (Gd, Y) sites and the Nb sites do not differ by much and one might observe a high symmetry pattern as an artifact (for example, the electron counts at the (Gd,Y) site of $Gd_{0.6}Y_{2.4}NbO_7$ is 44 which is close to the corresponding value of 41 for the Nb site). With the better resolution patterns of $Gd_{1.2}Y_{1.8}NbO_7$ and $Gd_{0.6}Y_{2.4}NbO_7$ obtained using the PANalytical diffractometer, we were able to observe the very weak superstructure peaks. It was interesting to find that although these weak superstructure peaks confirmed the C-centered orthorhombic unit cell, refinements in $C222_1$ did not converge. A search for higher symmetry yielded *Ccmm* with 0.5 Å tolerances on the search. Subsequent refinements of the structure in *Ccmm* proceeded smoothly and satisfactorily.

2.4. Reference X-ray powder pattern preparation

Reference X-ray patterns of selected members of $Ba_2(Gd_xY_{1-x})NbO_6$ (x=0.2, 0.4, 0.6, and 0.8) and of $(Gd_xY_{3-x})NbO_7$ (x=0.6, 1.2, 1.8, 2.4 and 3) were prepared using a Rietveld pattern decomposition technique. These patterns represent ideal specimen patterns. They are corrected for systematic errors in both *d* and *I*. The reported peak positions are calculated from the refined lattice parameters, as these positions represent the best measure of the true positions. For peaks resolved at the instrument resolution function, the individual peak positions are reported. For overlapping peaks, the intensity-weighted average peak position is reported with multiple indices. For marginally-resolved peaks, individual peaks are reported to more accurately simulate the visual appearance of the pattern.

2.5. Differential thermal analysis/thermogravimetric analysis (DTA/TGA)

Simultaneous differential thermal analysis and thermogravimetric analysis (DTA/TGA) were used to study thermal events. Most experiments utilized mainly the DTA signal; the TGA signal was useful primarily in following oxygen gain/loss associated with the CuO_γ component. DTA/TGA experiments were performed using an electronically upgraded Mettler TA-1 system fitted with an Anatech digital control and readout system. The DTA/TGA apparatus was calibrated against the α/β quartz transition (571 °C) and the melting point of NaCl (801 °C), and temperatures reported in this study have a standard uncertainty of ± 5 °C. Event temperatures were determined as the intersection of the baseline with the extrapolated linear portion of the rising DTA peak. Oxygen partial pressure during DTA/TGA was controlled using a previously analyzed Ar/O_2 mixture. During the experiments, gas was continuously flowed through the sample region at a rate of 150 mℓ/min, and the oxygen pressure at the outlet of the DTA/TGA system was periodically checked with a zirconia sensor.

3. Results and discussion

3.1. Chemical interactions of $Ba_2YCu_3O_{6+y}$ and Gd_3NbO_7

X-ray diffraction patterns of the two series of $Ba_2YCu_3O_{6+y}$/Gd_3NbO_7 samples prepared under 0.21 MPa p_{O_2} and 100 Pa p_{O_2} showed that the phases produced as a result of chemical reactions are similar, except that the phase CuO, which is stable at 0.21 MPa p_{O_2}, is replaced by Cu_2O at the more reduced condition of 100 Pa p_{O_2}. Because of the strong tendency of solid solution formation between $Ba_2(Y,Gd)Cu_3O_{6+y}$ and $(Gd,Y)_3NbO_7$, it is difficult to retain the single phases of $Ba_2YCu_3O_{6+y}$ and Gd_3NbO_7 once these two compounds are placed in contact with each other. Extensive solid solution formation was determined to be between Y and Gd sites in most of the compounds in the $BaO-\frac{1}{2}Y_2O_3-\frac{1}{2}Gd_2O_3-Nb_2O_5-CuO_y$ system because of the relatively small differences in ionic radius of Y^{3+} (1.019 Å) and Gd^{3+} (1.053 Å) [22,23].

In the phase diagrams of the BaO–Gd_2O_3–CuO [24] and BaO–Y_2O_3–CuO_γ [25] systems, $Ba_2YCu_3O_{6+y}$ is in equilibrium with $Y_2Cu_2O_5$, Cu_2O (CuO), and BaY_2CuO_5 phases, while $Ba_2GdCu_3O_{6+y}$ is in equilibrium with Gd_2CuO_4, Cu_2O (CuO), and $BaGd_2CuO_5$ phases instead. As expected, we found $(Y,Gd)_2Cu_2O_5$, Cu_2O (CuO),

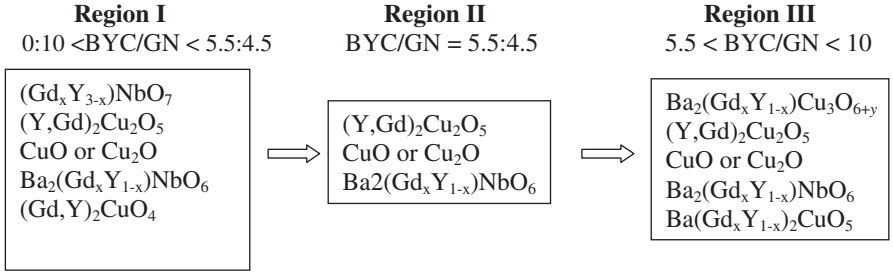

Fig. 1. A schematic representation of three regions of phase assemblages as a function of the compositional ratio of $Ba_2YCu_3O_{6+y}$ (BYC)/Gd_3NbO_7 (GN).

Table 2
Refinement residuals for $Ba_2(Gd_xY_{1-x})NbO_6$.

Space Group, SG	$Ba_2(Gd_{0.2}Y_{0.8})NbO_6$		$Ba_2(Gd_{0.4}Y_{0.6})NbO_6$		$Ba_2(Gd_{0.6}Y_{0.4})NbO_6$		$Ba_2(Gd_{0.8}Y_{0.2})NbO_6$	
	*Fm*3*m*	*I*4/*m*	*Fm*3*m*	*I*4/*m*	*Fm*3*m*	*I*4/*m*	*Fm*3*m*	*I*4/*m*
SG #	25	87	225	87	225	87	225	87
R_{wp}	0.0642		0.0550	0.0544	0.0483		0.0470	0.0446
R_p	0.0499		0.0428	0.0425	0.0377		0.0359	0.0348
χ^2	2.897	~2.91	2.410	2.365	2.157	~2.09	2.321	2.115
% χ^2 from restraints	0.05		0.08	0.51	0.14		0.003	1.48
# Variable	19		19	21	19		19	20
# Observ.	18504		18504	18504	18504		18504	18504
$R(F)$	0.0767		0.0954	0.0926	0.1023		0.1071	0.1074
$R(F)^2$	0.0936		0.0919	0.0746	0.0965		0.0791	0.0932
ΔF, +	4.5		3.7	3.1	3.1		9.7	7.8
ΔF, −	−1.9		−2.2	−2.5	−2.0		−3.5	−2.5
V_b								
Gd	3.86		3.82	3.98	3.82		3.60	4.04
Y	3.36		3.33	3.47	3.33		3.13	3.81
Nb	4.81		4.78	4.60	4.72		4.94	4.36
Impurity	0.8% $(Gd,Y)_2O_3$		0.8% $(Gd,Y)_2O_3$		0.8% $(Gd,Y)_2O_3$		1.3% $(Gd,Y)_2O_3$	
Phases	0.8% $(Gd,Y)NbO_{5.5}$		0.6% $(Gd,Y)NbO_{5.5}$		0.9% $(Gd,Y)NbO_{5.5}$			

Table 3
Crystallographic data for $Ba_2(Gd_xY_{1-x})NbO_6$, space group $Fm\bar{3}m$, D_x refers to calculated density, SOF refers to site occupancy fraction.

Compounds	a (Å)	V(Å^3)	D_x (g cm^{-3})	x (O5)	Gd_2/Y_3 SOF
$Ba_2Gd_{0.2}Y_{0.8}NbO_6$	8.44155(3)	601.54	6.251	0.2361(7)	0.20/0.8
$Ba_2Gd_{0.4}Y_{0.6}NbO_6$	8.45313(4)	604.02	6.376	0.2360(7)	0.40(2)/0.6(2)
$Ba_2Gd_{0.6}Y_{0.4}NbO_6$	8.46398(5)	606.35	6.501	0.2362(7)	0.62(2)/0.38(2)
$Ba_2Gd_{0.8}Y_{0.2}NbO_6$	8.47453(6)	608.62	6.626	0.2340(7)	0.91(3)/0.09(3)

The U_{iso} data have been deposited. The coordinates for Ba, Gd/Y, Nb and O are ($(\frac{1}{4},\frac{1}{4},\frac{1}{4})$, $(\frac{1}{2},\frac{1}{2},\frac{1}{2})$, (0,0,0), and ($x$,0,0)), respectively.

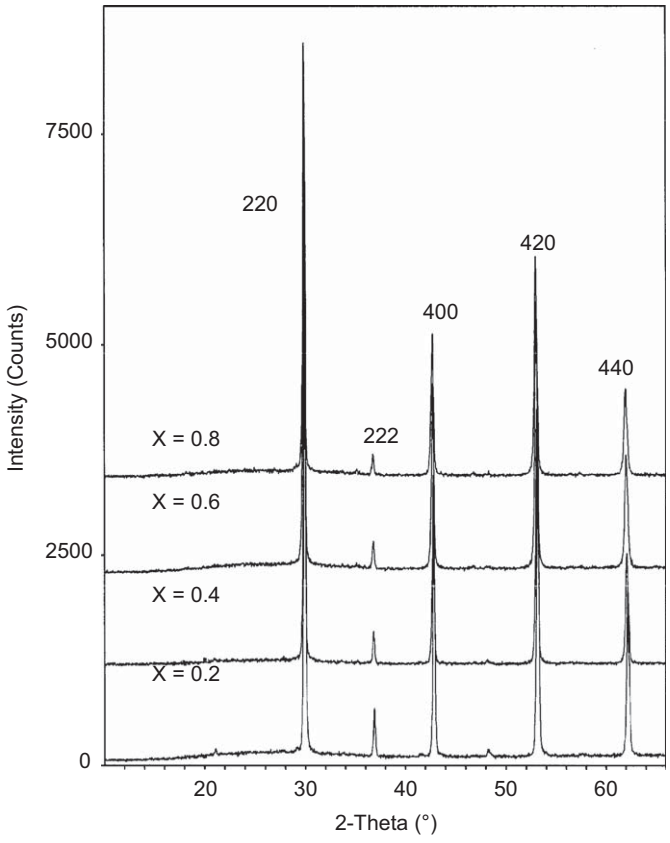

Fig. 2. X-ray diffraction patterns for the solid solution series $Ba_2(Gd_xY_{1-x})NbO_6$.

and $Ba(Y,Gd)_2CuO_5$, and $(Gd,Y)_2CuO_4$ phases as reaction products between $Ba_2YCu_3O_{6+y}$ and Gd_3NbO_7. Two additional products were determined to be $Ba_2(Gd_xY_{1-x})NbO_6$ and $(Gd_xY_{3-x})NbO_7$. Apparently Gd can substitute in the Y site of the $Y_2Cu_2O_5$ phase, while Y can substitute in the Gd site of the Gd_2CuO_4 phase to form solid solutions, as well.

Compositions that we studied all consist of phases belonging to five-phase volumes of the multi-component $BaO-\frac{1}{2}Y_2O_3-\frac{1}{2}Gd_2O_3-Nb_2O_5-CuO_y$ system. Since it is difficult to delineate a 5-dimensional phase diagram, a schematic diagram representing the progression of the interactions between $Ba_2YCu_3O_{6+y}$ and Gd_3NbO_7 is shown in Fig. 1. Starting from the $Ba_2YCu_3O_{6+y}$-poor region (ratio of $Ba_2YCu_3O_{6+y}/Gd_3NbO_7$=1:9) to the $Ba_2YCu_3O_{6+y}$-rich region ($Ba_2YCu_3O_{6+y}/Gd_3NbO_7$=9:1), one observes a progressive change of the intensity in the X-ray diffraction patterns of respective phases. In general, the two five-phase regions and one three-phase region can be described as follows:

Region I: 0:10 < $Ba_2YCu_3O_{6+y}$: Gd_3NbO_7 < 5.5:4.5, the five phases present are $(Gd_xY_{3-x})NbO_7$, $(Gd,Y)_2CuO_4$, $(Y,Gd)_2Cu_2O_5$, CuO/Cu_2O and $Ba_2(Gd_xY_{1-x})NbO_6$
Region II: $Ba_2YCu_3O_{6+y}$: Gd_3NbO_7=5.5:4.5, only three phases present. This region defines the common three phase region of $(Y,Gd)_2Cu_2O_5$, CuO/Cu_2O and $Ba_2(Gd_xY_{1-x})NbO_6$
Region III: 5.5:4.5 < $Ba_2YCu_3O_{6+y}$: Gd_3NbO_7 < 10: 0, the five phases present are $Ba_2(Y,Gd)Cu_3O_{6+y}$, $Ba(Y,Gd)_2CuO_5$, $(Y,Gd)_2Cu_2O_5$, CuO/Cu_2O and $Ba_2(Gd_xY_{1-x})NbO_6$

The minimum melting temperatures obtained from the DTA experiments for each of the compositions of the $Ba_2YCu_3O_{6+y}/Gd_3NbO_7$ mixtures prepared under purified air occur from 938 to 1037 °C for ratios of 1:9 to 9:1, respectively. These melting temperatures are lower than those for $Ba_2YCu_3O_{6+y}$ (1015 °C [26]) and Gd_3NbO_7 (> 1400 °C [27]).

3.2. Crystal structure of $Ba_2(Gd_xY_{1-x})NbO_6$ and $(Gd_xY_{3-x})NbO_7$

3.2.1. $Ba_2(Gd_xY_{1-x})NbO_6$

Table 2 gives the Reitveld refinement residuals for $Ba_2(Gd_xY_{1-x})NbO_6$ (cubic $Fm\bar{3}m$ and *I*4/*m*). Using the *I*4/*m* model, cell refinement for $Ba_2Gd_{0.2}Y_{0.8}NbO_6$ and $Ba_2Gd_{0.6}Y_{0.4}NbO_6$ did not converge even with heavy damping of the lattice parameters. The data on the three Y-rich compounds do not support refining the structure in the

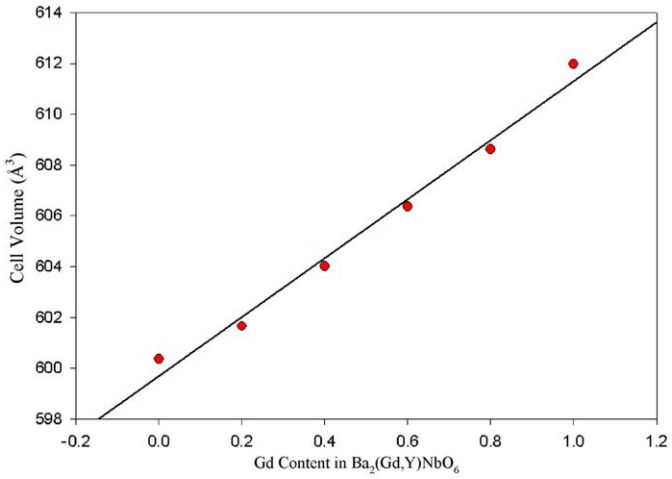

Fig. 3. Plot of cell volume of $Ba_2(Gd_xY_{1-x})NbO_6$ *vs x*. A monotonic trend is observed.

Table 4
Bond distances and bond valence sum (V_b) [20,21] in $Ba_2(Gd_xY_{1-x})NbO_6$, space group $Fm\bar{3}m$.

Bond type	Distances (Å)	V_b	Bond type	Distances (Å)	V_b
(1) $Ba_2Gd_{0.2}Y_{0.8}NbO_6$					
Ba–O	2.9868(2) × 12	1.825	Gd/Y–O	2.2286(6) × 6	3.458
Nb–O	1.993(6) × 6	4.807			
(2) $Ba_2Gd_{0.4}Y_{0.6}NbO_6$					
Ba–O	2.9910(2) × 12	1.804	Gd/Y–O	2.232(6) × 6	3.526
Nb–O	1.995(6) × 6	4.781			
(3) $Ba_2Gd_{0.6}Y_{0.4}NbO_6$					
Ba–O	2.9947(2) × 12	1.787	Gd/Y–O	2.232(6) × 6	3.526
Nb–O	2.000(6) × 6	4.717			
(4) $Ba_2Gd_{0.8}Y_{0.2}NbO_6$					
Ba–O	2.9993(2) × 12	1.7645	Gd/Y–O	2.254(6) × 6	3.507
Nb–O	1.983(6) × 6	4.939			

V_b values for the (Gd,Y) sites were computed based on the corresponding site occupancy.

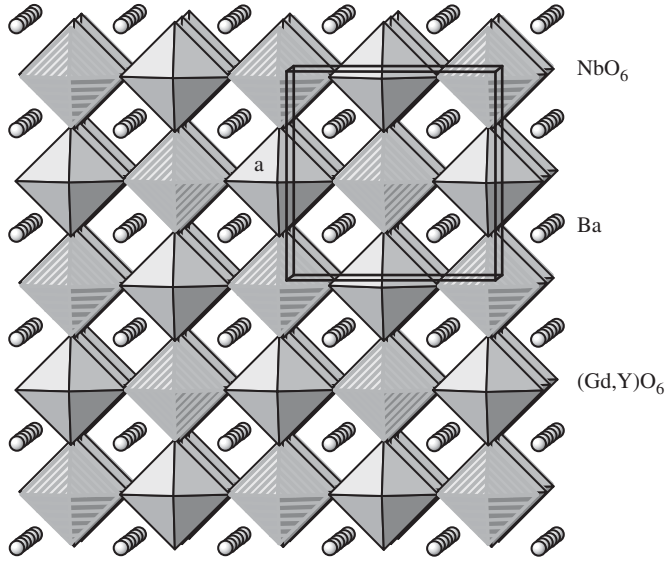

Fig. 4. Crystal structure of $Ba_2(Gd_xY_{1-x})NbO_6$ showing the corner sharing NbO_6 octahedra (ruled pattern) and $(Gd,Y)O_6$ octahedra (plain pattern).

tetragonal $I4/m$ model. The refinement of the Y-poor phase, $Ba_2Gd_{0.8}Y_{0.2}NbO_6$ in $I4/m$ converged only with heavy damping. Slightly lower residuals were obtained than for the $Fm\bar{3}m$ model, but the bond valence sums for Gd,Y, and Nb are much more reasonable for the $Fm\bar{3}m$ model. Any distortions from the cubic symmetry in this compound must be small. Any out-of-plane tilt are being masked by cation ordering. It is therefore best to discuss the systematics of the $Ba_2(Gd_xY_{1-x})NbO_6$ phases in the followings using the cubic $Fm\bar{3}m$ symmetry.

Table 3 provides the cubic lattice parameters of $Ba_2(Gd_xY_{1-x})NbO_6$ and the x coordinates for O_5. Fig. 2 gives the series of X-ray patterns for four compositions of the $Ba_2(Gd_xY_{1-x})NbO_6$ solid solutions, namely, $Ba_2(Gd_{0.8}Y_{0.2})NbO_6$, $Ba_2(Gd_{0.6}Y_{0.4})NbO_6$, $Ba_2(Gd_{0.4}Y_{0.6})NbO_6$, and $Ba_2(Gd_{0.2}Y_{0.8})NbO_6$, with selected indices provided. Fig. 3 shows the plot of lattice parameters vs. x. Since the ionic radius of Gd^{3+} (1.053 Å) is greater than that of Y^{3+} (1.019 Å) [22,23], a monotonic increase of cell parameters as x increases is observed.

Table 4 lists the bond distances for the structure of $Ba_2(Gd_xY_{1-x})NbO_6$, respectively. As reported by Brixner [28], there may be a complication in the structure of the solid solution, as Y and Nb, or Gd and Nb can potentially substitute each other as well. We established that no visible extra X-ray diffraction peaks were found in the patterns of the $Ba_2(Gd_xY_{1-x})NbO_6$ solid solution members. $Ba_2(Gd_xY_{1-x})NbO_6$ was found to be isostructural to A_2EuNbO_6 (where A=Ba, Sr, and Ca), which adopts an ordered perovskite structure ([29,30]). No substitution of Eu on Nb nor Ta site was reported.

Fig. 4 gives the structure of $Ba_2(Gd_xY_{1-x})NbO_6$, which consists of corner-sharing NbO_6 and $(Gd,Y)O_6$ octahedra, with Ba situated in the 12-coordinated cage. The V_b values for Ba, Gd/Y, and Nb are also included in Table 2 [20,21]. The V_b values for the mixed (Gd,Y) sites were computed based on the corresponding site occupancy. Note that the V_b values for Nb (ranging from 4.72 to 4.93) do not deviate significantly from the ideal value of 5.0. However, the V_b values for the Gd/Y sites in all four compounds (ranging from 3.46 to 3.53) are much greater than the ideal value of 3.0. These high values indicate large compressive stress (overbonding, or the cages in which Gd/Y reside are too small). While the V_b values for the Ba site are all less than the ideal value of 2 (underbonding, tensile stress, or atom in an oversized cage), they decrease further from 1.825(x=0.2) to a small value of 1.764 (x=0.8). Oversized cages for alkaline-earth elements such as Ba and Sr have been found in other compounds [31,32].

3.2.2. $(Gd_xY_{3-x})NbO_7$

As mentioned earlier, results of our Rietveld refinements show the X-ray data of members of $(Gd_xY_{3-x})NbO_7$ solid solution to be best fitted to the $Ccmm$ and $C222_1$ space groups. Table 5 gives the

Table 5
$Gd_{3-x}Y_xNbO_7$ rietveld refinement residuals.

Formula (x)	0	0.6	1.2	1.8	2.4
Space Group	$C222_1$	$C222_1$	$C222_1$	$Ccmm$	$Ccmm$
wR_p	0.0570	0.0537	0.0456	0.0561	0.0583
R_p	0.0422	0.0400	0.0352	0.0391	0.0394
χ^2	3.689	2.917	2.809	4.101	5.080
% χ^2 from restraints	26	5.5	24	7.7	7.5
#Variables	37	38	37	33	39
# Observ.	9639	9614	9644	9643	9643
$R(F)$	0.0750	0.0764	0.0533	0.1407	0.1581
$R(F^2)$	0.0755	0.0724	0.0672	0.0675	0.0619
ΔF, + e Å^{-3}	5.3	2.2	1.4	4.4	5.3
–	−5.3	−3.8	−3.2	−7.6	−7.8
impurities	–	–	4.4% $GdNbO_4$	–	1.1% $YNbO_4$

refinement residues. Table 6 provides the lattice parameters of $(Gd_xY_{3-x})NbO_7$. Tables 7 and 8 tabulate the atomic coordinates and bond distances for the solid solution members of $(Gd_xY_{3-x})NbO_7$, respectively. Fig. 5 gives observed (crosses) and calculated (solid line) XRD intensities pattern for $Gd_{2.4}Y_{0.6}NbO_7$ at 295 K. The difference pattern is plotted at the same scale as the other patterns. The thick marks indicate the calculated peak positions for $Gd_{2.4}Y_{0.6}NbO_7$. Fig. 6 illustrates the plot of unit cell volume vs. x in $(Gd_xY_{3-x})NbO_7$. A monotonic increase of cell parameters as x increases is discernible, as expected.

Table 6
Lattice parameters for $(Gd_xY_{3-x})NbO_7$.

x	a (Å)	b (Å)	c(Å)	Space group	V (Å^3)
0.6	10.52347(17)	7.44153(11)	7.4599 (2)	*Ccmm* (No. 63)	584.19(2)
1.2	10.5477(3)	7.45977(13)	7.4829(2)	*Ccmm* (No. 63)	588.78(2)
1.8	10.5564(2)	7.47822(14)	7.51625(14)	$C222_1$ (No. 20)	593.36(2)
2.4	10.5804 (2)	7.50007(11)	7.53437(9)	$C222_1$ (No. 20)	597.88(2)
3.0	10.61073(8)	7.52852(7)	7.54916(5)	$C222_1$ (No. 20)	603.050(8)

In the fluorite-related structure of $(Gd_xY_{3-x})NbO_7$ (*Ccmm*, $C222_1$) [9,33], there are two distinct (Gd, Y) sites. One-third of the (Gd,Y) cations are 8-fold coordinated, and the remainder are 7-fold coordinated. The $(Gd,Y)O_8$ polyhedra occupy positions in [001] rows which alternate with parallel rows of corner-shared MO_6 coordination octahedra. Fig. 7 gives the layered feature of the alternate stacking of distorted NbO_6 octahedral chains and $(Gd,Y)O_8$ polyhedra perpendicular to the a-axis (the $(Gd,Y)O_7$ polyhedra are not shown). The 7-fold coordinated (Gd,Y) cations, which form seven of the eight vertices of a distorted cube, lie in between the slabs that are perpendicular to the a-axis. Fig. 8 shows the relations between the NbO_6 octahedral chains and the $(Gd,Y)O_7$ polyhedra. For clarity, the $(Gd,Y)O_8$ polyhedra are not shown.

The V_b values [20,21] (Table 8) for the 8-coordinated $(Gd,Y)O_8$ sites indicated most of the sites are slightly overbonded (an average of V_b of 3.143 among the five phases). On the other hand, most of the 7-coordinated $(Gd,Y)O_7$ sites are slightly under tensile stress (an average of V_b of 2.961). As the Gd content of the samples increases, the Nb sites are becoming stress free (V_b values run from 4.593 to 5.060, close to the ideal value of '5').

Table 7
Atomic coordinates for $(Gd_xY_{1-x})_3NbO_7$.

Atom site	x	y	z	SOF	U_{iso}	Wy Sym
(1) $Gd_{0.6}Y_{2.4}NbO_7$ (*Ccmm*)						
Gd1/Y2	0.5	0.0	0.5	0.106 (6)/0.894	0.0261 (4)	4*b*
Gd3/Y4	0.24618 (26)	−0.2517 (5)	−0.25	0.294 (6)/0.706	0.0261 (4)	8*g*
Nb5	0.0	0.0	0.5	1.0	0.0111 (9)	4*a*
O6	0.1156 (7)	−0.2155 (9)	0.4707 (13)	1.0	0.0268 (14)	16*h*
O7	0.6281 (20)	0.0	−0.25	1.0	0.0268 (14)	4*c*
O8	0.3741 (20)	0.0	−0.25	1.0	0.0268 (14)	4*c*
O9	0.0640 (15)	0.0	−0.25	1.0	0.0268 (14)	4*c*
(2) $Gd_{1.2}Y_{1.8}NbO_7$ (*Ccmm*)						
Gd1/Y2	0.5	0.0	0.5	0.322 (8)/0.678	0.0244 (4)	4*b*
Gd3/Y4	0.24233 (19)	−0.24369 (31)	−0.25	0.478 (8)/0.522	0.0244 (4)	8*g*
Nb5	0.0	0.0	0.5	1.0	0.0031 (7)	4*a*
O6	0.1145 (7)	−0.2097 (8)	0.4683 (10)	1.0	0.0178 (14)	16*h*
O7	0.630 (2)	0.0	−0.25	1.0	0.0178 (14)	4*c*
O8	0.369 (2)	0.0	−0.25	1.0	0.0178 (14)	4*c*
O9	0.0615 (15)	0.0	−0.25	1.0	0.0178 (14)	4*c*
(3) $Gd_{1.8}Y_{1.2}NbO_7$ ($C222_1$)						
Gd1/Y2	0.0	0.5107 (7)	0.25	0.751 (7)/0.249	0.0280 (3)	4*b*
Gd3/Y4	0.23363 (11)	0.2366 (3)	0.0053 (4)	0.523 (6)/0.477	0.0280 (3)	8*c*
Nb5	0.0	−0.0035 (5)	0.25	1.0	0.0048 (6)	4*b*
O6	0.1361 (6)	0.1728 (10)	0.2895 (6)	1.0	0.0205 (12)	8*c*
O7	0.1109 (4)	−0.2167 (6)	0.2714 (6)	1.0	0.0205 (12)	8*c*
O8	0.1222 (5)	0.5	0.0	1.0	0.0205 (12)	4*a*
O9	0.1238 (4)	0.5	0.5	1.0	0.0205 (12)	4*a*
O10	0.0542 (4)	0.0	0.0	1.0	0.0205 (12)	4*a*
(4) $Gd_{2.4}Y_{0.6}NbO_7$ ($C222_1$, No. 20)						
Gd1	0.0	0.5111 (7)	0.25	1.0	0.02250 (30)	4*b*
Gd3/Y4	0.23241 (10)	0.2348 (3)	0.0069 (3)	0.7/0.3	0.02250 (30)	8*c*
Nb5	0.0	−0.0028 (8)	0.25	1.0	0.0103 (7)	4*b*
O6	0.1274 (11)	0.184 (2)	0.2897 (12)	1.0	0.0278 (15)	8*c*
O7	0.1133 (9)	−0.2107 (11)	0.2821 (9)	1.0	0.0278 (15)	8*c*
O8	0.1196 (12)	0.5	0.0	1.0	0.0278 (15)	4*a*
O9	0.1281 (11)	0.5	0.5	1.0	0.0278 (15)	4*a*
O10	0.0667 (9)	0.0	0.0	1.0	0.0278 (15)	4*a*
(5) Gd_3NbO_7 ($C222_1$)						
Gd1	0.0	0.5161 (5)	0.25	1.0	0.0168 (3)	4*b*
Gd3	0.23107 (9)	0.2331 (2)	0.0076 (3)	1.0	0.0168 (3)	8*c*
Nb5	0.0	−0.0046 (6)	0.25	1.0	0.0072 (7)	4*b*
O6	0.1346 (6)	0.1703 (11)	0.2893 (6)	1.0	0.023(2)	8*c*
O7	0.1119 (8)	−0.2143 (6)	0.2741 (6)	1.0	0.023 (2)	8*c*
O8	0.1221 (6)	0.5	0.0	1.0	0.023 (2)	4*a*
O9	0.1242 (5)	0.5	0.5	1.0	0.023 (2)	4*a*
O10	0.0599 (5)	0.0	0.0	1.0	0.023 (2)	4*a*

The Wyckoff symbol (Wy Sym) is also given. SOF refers to site occupancy fraction.

Table 8
Bond distances and bond valence sum (V_b) [20,21] in $(Gd_xY_{1-x})_3NbO_7$.

Bond type	Distances (Å)	V_b
(1) $Gd_{0.6}Y_{2.4}NbO_7$ (*Ccmm*)		
Gd1/Y2–O6	2.451 (8) × 4	3.151
Gd1/Y2–O7	2.301 (12) × 2	
Gd1/Y2–O8	2.288 (12) × 2	
Gd3/Y4–O6	2.511 (9) × 2	3.002
Gd3/Y4–O6	2.211 (8) × 2	
Gd3/Y4–O7	2.227 (12)	
Gd3/Y4–O8	2.307 (13)	
Gd3/Y4–O9	2.680 (12)	
Nb5–O6	2.024 (5) × 4	4.593
Nb5–O9	1.983 (5) × 2	
(2) $Gd_{1.2}Y_{1.8}NbO_7$ (*Ccmm*)		
Gd1/Y2–O6	2.491 (8) × 4	2.980
Gd1/Y2–O7	2.319 (12) × 2	
Gd1/Y2–O8	2.324 (12) × 2	
Gd3/Y4–O6	2.515 (8) × 2	2.999
Gd3/Y4–O6	2.252 (7) × 2	
Gd3/Y4–O7	2.249 (11)	
Gd3/Y4–O8	2.258 (12)	
Gd3/Y4–O9	2.635 (11)	
Nb5–O6	1.990 (5) × 4	4.891
Nb5–O9	1.980 (5) × 2	
(3) $Gd_{1.8}Y_{1.2}NbO_7$ ($C222_1$)		
Gd1/Y2–O6	2.922 (8) × 2	3.206
Gd1/Y2–O7	2.356 (3) × 2	
Gd1/Y2–O8	2.281 (3) × 2	
Gd1/Y2–O9	2.290 (3) × 2	
Gd3/Y4–O6	2.419 (4)	2.891
Gd3/Y4–O6	2.232 (4)	
Gd3/Y4–O7	2.455 (4)	
Gd3/Y4–O7	2.373 (4)	
Gd3/Y4–O8	2.295 (3)	
Gd3/Y4–O9	2.323 (3)	
Gd3/Y4–O10	2.592 (3)	
Nb5–O6	1.973 (2) × 2	5.060
Nb5–O7	1.985 (2) × 2	
Nb5–O10	1.9644 (13) × 2	
(4) $Gd_{2.4}Y_{0.6}NbO_7$ ($C222_1$)		
Gd1/Y2–O6	2.815 (14) × 2	3.180
Gd1/Y2–O7	2.419 (9) × 2	
Gd1/Y2–O8	2.270 (7) × 2	
Gd1/Y2–O9	2.322 (7) × 2	
Gd3/Y4–O6	2.434 (9)	2.947
Gd3/Y4–O6	2.291 (9)	
Gd3/Y4–O7	2.522 (7)	
Gd3/Y4–O7	2.315 (8)	
Gd3/Y4–O8	2.321 (7)	
Gd3/Y4–O9	2.298 (8)	
Gd3/Y4–O10	2.486 (7)	
Nb–O6	1.967 (6) × 2	4.896
Nb–O7	1.982 (6) × 2	
Nb–O10	2.011 (3) × 2	
(5) Gd_3NbO_7 ($C222_1$)		
Gd1–O6	2.984 (10) × 2	3.199
Gd1–O7	2.359 (4) × 2	
Gd1–O8	2.292 (3) × 2	
Gd1–O9	2.305 (3) × 2	
Gd3–O6	2.407 (4)	2.966
Gd3–O6	2.297 (4)	
Gd3–O7	2.478 (4)	
Gd3–O7	2.377 (4)	
Gd3–O8	2.319 (3)	
Gd3–O9	2.333 (4)	
Gd3–O10	2.526 (4)	
Nb–O6	1.965 (2) × 2	4.977
Nb–O7	1.984 (2) × 2	
Nb–O10	1.992 (2) × 2	

The V_b values for the (Gd,Y) sites were computed based on the corresponding site occupancy fraction.

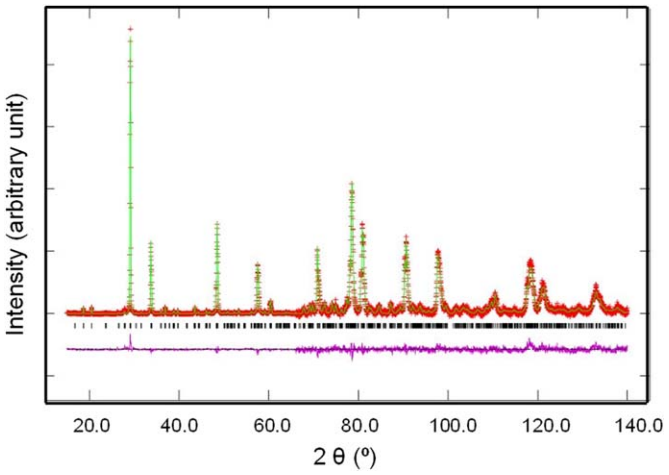

Fig. 5. Observed (crosses) and calculated (solid line) XRD intensities pattern for $Gd_{2.4}Y_{0.6}NbO_7$ at 295 K. The difference pattern is plotted at same scale as the other patterns. The thick marks indicate the calculated peak positions for $Gd_{2.4}Y_{0.6}NbO_7$.

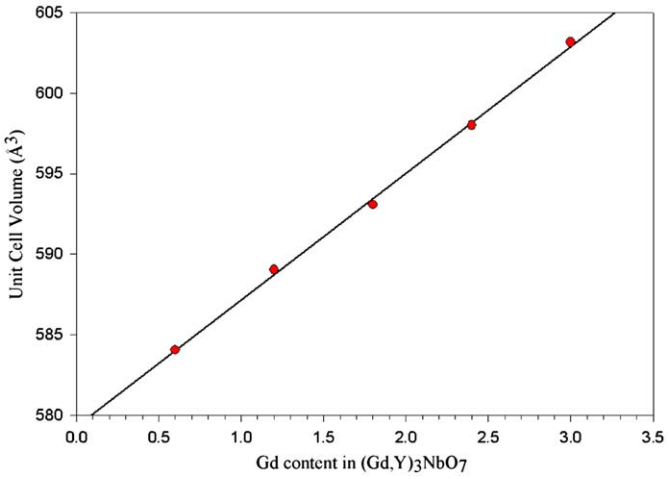

Fig. 6. Plot of cell volume of $(Gd_xY_{3-x})NbO_7$ *vs. x*. A monotonic trend is observed.

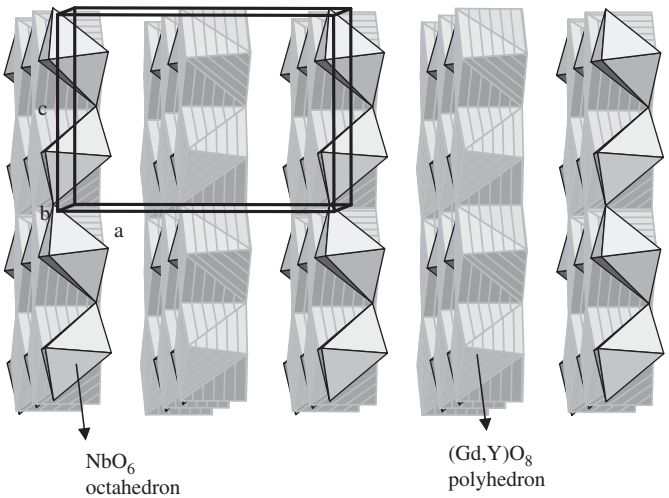

Fig. 7. Crystal structure for Gd_3NbO_7 ($C222_1$) showing the partial layered feature. The alternate stacking of distorted NbO_6 octahedra (plain pattern) and $(Gd,Y)O_8$ polyhedra (ruled pattern) are illustrated. The $(Gd,Y)O_7$ polyhedra are omitted for clarity.

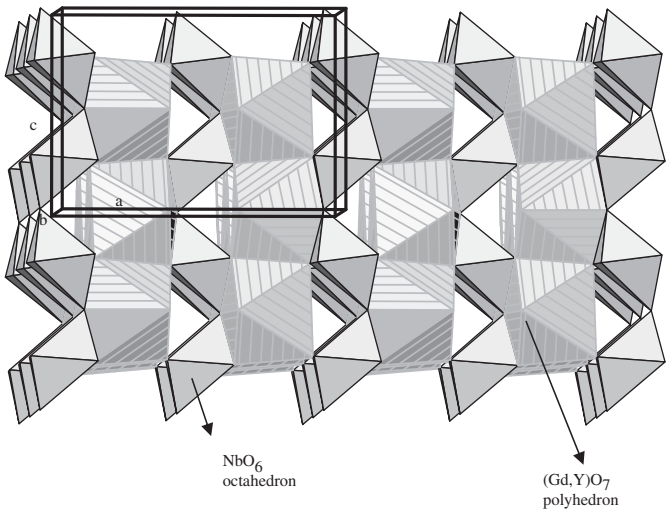

Fig. 8. Crystal structure for Gd_3NbO_7 ($C222_1$) showing the partial layered feature. The alternate stacking of distorted NbO_6 octahedra (plain pattern) and $(Gd,Y)O_7$ polyhedra (ruled pattern) are illustrated. The $(Gd,Y)O_8$ polyhedra are omitted for clarity.

Table 9
X-ray powder pattern for $Ba_2(Gd_{0.6}Y_{0.4})NbO_6$, $Fm\bar{3}m$, a=8.46398(5) Å, and V=606.35 Å^3, Z=4.

d	I	h	k	l	D	I	h	k	l	d	I	h	k	l
4.8867	12	1	1	1	2.9925	999*	2	2	0	2.5520	5	3	1	1
2.4433	37	2	2	2	2.1160	315	4	0	0	1.9418	5	3	3	1
1.7278	443	4	2	2	1.4962	187	4	4	0	1.3383	175	6	2	0
1.2760	4	6	2	2	1.2217	54	4	4	4	1.1310	214	6	4	2
1.0580	26	8	0	0	0.9975	127	6	6	0M	0.9975	127	8	2	2M
0.9463	101	8	4	0	0.9023	78	6	6	4	0.8639	99	8	4	4
0.8300	302	10	2	0M	0.8300	302	8	6	2M					

The symbols 'M' and '+' refer to peaks containing contributions from two and more than two reflections, respectively. The symbol * indicates the particular peak has the strongest intensity of the entire pattern and is designated a value of '999'.

The NbO_6 octahedra in the reported $C222_1$ structure of Gd_3NbO_7 [9] and our data both exhibit significant distortion. The average deviations from the ideal O–Nb–O angles are 8.8(52)° in [9] and 6.4(31)° in our refined structure of Gd_3NbO_7. To explore the distortion further, the $C222_1$ structure was converted to $P1$ and optimized using VASP [34–36] with fixed lattice parameters. The symmetry of the optimized structure gives $C222_1$ to within 0.001 Å, providing good evidence that this space group is correct. In $P1$, the geometries of the 4 independent Nb are identical, and the average deviation from the ideal octahedral angles is 6.1(26)°. Therefore the observed distortions are what one would expect.

3.2.3. Powder diffraction patterns for PDF

We have prepared the powder X-ray reference patterns for four $Ba_2(Gd_xY_{1-x})NbO_6$ phases (x=0.2, 0.4, 0.6, and 0.8) and also for five $(Gd_xY_{3-x})NbO_7$ (x=0.6, 1.2, 1.8, 2.4, and 3.0) phases. Table 9 gives an example of the selected pattern for $Ba_2(Gd_{0.6}Y_{0.4})NbO_6$. In this pattern, the symbols 'M' and '+' refer to peaks containing contributions from two and more than two reflections, respectively. The symbol * indicates that the particular peak has the strongest intensity of the entire pattern and has been designated a value of '999'. The intensity values reported are integrated intensities rather than peak heights. All patterns have been submitted for inclusion in the Powder Diffraction File (PDF).

4. Summary

The chemical interaction between $Ba_2YCu_3O_{6+y}$ and Gd_3NbO_7 has been investigated. Two different five-phase regions were found along the pseudo-binary path between $Ba_2YCu_3O_{6+y}$ and Gd_3NbO_7. The crystal structures of two specific reaction products, $Ba_2(Gd_xY_{1-x})NbO_6$ and $(Gd_xY_{3-x})NbO_7$, have been investigated by X-ray powder diffraction. The structure of $Ba_2(Gd_xY_{1-x})NbO_6$ was determined to be cubic $Fm\bar{3}m$, and the structure of the $(Gd_xY_{3-x})NbO_7$ solid solution members were found to crystallize in the space group of $C222_1$ and $Ccmm$. Knowledge of these reaction products provides a reference for the identification of second phases in the SEM or TEM micrographs of the interface between the $Ba_2YCu_3O_{6+y}$ superconductor film and the Gd_3NbO_7 buffer layer. Work continues on the study of interactions between $Ba_2YCu_3O_{6+y}$ and other potentially important buffer materials, such as $LaMnO_3$.

Acknowledgments

The partial financial support from the Office of Electricity Delivery and Energy Reliability of the US Department of Energy is acknowledged. Mr. N. Swanson and Dr. P. Schenck are thanked for their assistance in graphic presentations.

Appendix A. Supplementary data

Supplementary data associated with this article can be found in the online version at 10.1016/j.jssc.2010.01.006.

References

[1] S.R. Foltyn, E.J. Peterson, J.Y. Coulter, P.N. Arendt, Q.X. Jia, P.C. Dowden, M.P. Maley, X.D. Wu, D.E. Peterson, J. Mater. Res. 12 (1997) 2941–2946.
[2] M. Bauer, R. Semerad, H. Kinder, IEEE Trans. Appl. Supercond. 9 (2) (1999) 1502–1505.
[3] M.W. Rupich, W. Zhang, X. Li, T. Kodenkandath, D.T. Verebelyi, U. Schoop, C. Thieme, M. Teplitsky, J. Lynch, N. Nguyen, E. Siegal, J. Scudiere, V. Maroni, K. Venkataraman, D. Miller, T.G. Holesinger, Physica C 412-414 (2004) 877–884.
[4] X. Li, M.W. Rupich, W. Zhang, N. Nguyen, T. Kodenkandath, U. Schoop, D.T. Verebelyi, C. Thieme, M. Jowett, P.N. Arendt, S.R. Foltyn, T.G. Holesinger, T. Aytug, D.K. Christen, M.P. Paranthaman, Physica C 390 (2003) 249–253.
[5] W. Wong-Ng, L.P. Cook, P. Schenck, I. Levin, Z. Yang, Q. Huang, J. Frank, in: Proceedings of the PACRIM meeting, sponsored by ACerS, Maui, Hawaii, September, 2005; Ceramic Transactions, vol. 191, 2006, pp. 83–98.
[6] L.P. Cook, W. Wong-Ng, P. Schenck, Z. Yang, I. Levin, J. Frank, J. Electron. Mater. 36 (10) (2007) 1293–1298.
[7] K. Sato, H. Kiyokawa, G.-A. Adachi, J. Shiokawa, Inorg. Chem. 16 (2) (1977) 328–331.
[8] P.J. Saines, B.J. Kennedy, J. Solid State Chem. 181 (2) (2008) 298–305.
[9] J.G. Allpress, H.J. Rossell, J. Solid State Chem. 27 (1979) 105–114.
[10] G. Garton, B.M. Wanklyn, J. Mater. Sci. 3 (1968) 395–401.
[11] V.P. Sirotinkin, A.A. Evdokimov, V.K. Trunov, Russ. J. Inorg. Chem. 27 (7) (1982) 931–933.
[12] H.P. Rooksby, E.A.D. White, J. Am. Ceram. Soc. 47 (1964) 94–96.
[13] A.N. Klimenko, V.M. Lonov, N.A. Tomilin, V.S. Sergeev, V.P. Sirotinkin, A.E. Prozorovskii, V.B. Rybakov, S.G. Zhukov, Russ. J. Inorg. Chem. (Engl. Transl.) 35 (1990) 338.
[14] M.G. Safronenko, Y.E. Bogatov, A.K. Molodkin, Russ. J. Inorg. Chem. (Engl. Transl.) 37 (1992) 5.
[15] J.J. Ritter, Powd. Diff. 3 (1) (1988) 30–31.
[16] PDF, Powder Diffraction File, produced by International Centre for Diffraction Data (ICDD), 12 Campus Blvd., Newtown Square, PA, USA, 19073-3273.
[17] H.M. Rietveld, J. Appl. Cryst. 2 (1969) 65–71.

[18] R.A. Young (Ed.), The Rietveld Method, International Union of Crystallography Monograph on Crystallography, vol. 5, Oxford University Press, Oxford, 1993.
[19] A.C. Larson, R.B. von Dreele, GSAS-General Structure Analysis System, US Government contract (W-7405-ENG-36) by the Los Alamos National Laboratory, which is operated by the University of California for the US Department of Energy, 1992.
[20] N.E. Brese, M. O'Keeffe, Acta Crystallogr. B 47 (1991) 192–197.
[21] I.D. Brown, D. Altermatt, Acta Crystallogr. B 41 (1985) 244–247.
[22] R.D. Shannon, C.T. Prewitt, Acta Crystallogr. B 25 (1969) 925–946.
[23] R.D. Shannon, Acta Crystallogr. A 32 (1976) 751–767.
[24] W. Wong-Ng, L.P. Cook, J. Suh, J. Kaduk, Solid State Sci. 6 (2004) 1211–1216.
[25] W. Wong-Ng, J. Suh, L.P. Cook, Physica C 377 (2002) 107–113.
[26] W. Wong-Ng, L.P. Cook, J. Res. Natl. Inst. Stand. Technol. 103 (1998) 379.
[27] R.S. Roth, in: E.V. Leber (Ed.), Rare Earth Res. Semin., Lake Arrowhead, California, October 1960, Macmillan Publishing, Riverside, New Jersey, 1961, pp. 88–95.
[28] L.H. Brixner, J. Inorg. Nucl. Chem. 15 (1960) 352–355.
[29] V.S. Filip'ev, E.G. Fresenko, Kristallografiya 6 (1961) 770–772.
[30] K. Sato, H. Kiyokawa, G.-Y. Adachi, J. Shiokawa, Inorg. Chem. 16 (2) (1977) 328–331.
[31] W. Wong-Ng, T. Haugan, J.A. Kaduk, R.A. Young, Z. Yang, M.H. Jang, M. Luong, J. Solid State Chem. 179 (2006) 1588–1595.
[32] J.A. Kaduk, W. Wong-Ng, W. Greenwood, J. Dillingham, B.H. Toby, J. Res. Natl. Inst. Stand. Technol. 104 (1999) 147.
[33] H.J. Rossell, J. Solid State Chem. 27 (1979) 115–122.
[34] G. Kresse, J. Furthmüller, Phys. Rev. B 54 (1996) 11169.
[35] G. Kresse, J. Furthmüller, J. Comput. Mater. Sci. 6 (1996) 15.
[36] J. Hafner, J. Comput. Chem. 29 (2008) 2044–2078.